Selected Resonant Topologies for Non-wireless and Wireless Power Transfer

Rafał Kasikowski

Lodz University of Technology, Faculty of Electrical, Electronic, Computer and Control Engineering, Institute of Electronics, al. Politechniki 8, 93-590 Łódź

Abstract: Resonant topologies are extensively used across various sectors of the electronics industry owing to their intrinsic advantages, such as superior efficiency, high power density, electrical isolation, low electromagnetic interference (EMI) and harmonic distortion, feasibility of magnetic integration, reduced voltage stress, and operation at high frequencies. This paper presents two prominent resonant network configurations: a non-wireless LLC topology and an LCC-S resonant Wireless Power Transfer (WPT) architecture. The latter employs magnetic coupling to achieve efficient power transfer over a distance, usually ranging from a few millimetres to several or tens of centimetres, thereby eliminating the dependency on conventional wired connections. A detailed theoretical discussion of both resonant network designs is provided, along with an analysis of their respective merits and limitations. It is demonstrated that both topologies attain high power conversion efficiency through the implementation of zero voltage transition (ZVT). Furthermore, these topologies offer a substantial advantage over other resonant tank designs, as their output voltage remains essentially invariant to load fluctuations when the converter's switching frequency is precisely matched to the network's resonant frequency. The final section details the practical implementation of the integrated LLC resonant topology and investigates the effects of mismatch between the operational and resonant frequencies on current and voltage waveforms, gain characteristics, efficiency, and thermal performance.

Keywords: power electronics, resonant converters, wireless power transfer, load-independent operation, thermography

1. Introduction

Recent developments in high-frequency power converters have primarily been characterized by rapid improvements in power conversion efficiency. This improvement has often been accompanied by enhanced power density, resulting in a substantial reduction in the size of power supplies as well as a marked boost in energy efficiency. The rising demand for smaller, more efficient devices has driven a reconsideration of power supply design methodologies and a transition to topologies better suited for achieving high efficiency.

One major innovation broadening the scope of power converter applications is the ability to transfer power wirelessly, without a direct physical connection between the primary energy source and the end user. This technology, known as WPT, removes the limitation of a fixed physical link between the primary and secondary sides of power supplies, enabling more versatile products. Due to these benefits and enhanced user convenience, resonant topologies have become prevalent in modern medium- and high-power AC/DC converters. Conventional topologies, which do not deliver ultra-high energy efficiency or improved user convenience, are gradually being replaced by these more advanced solutions.

LLC resonant converters have been widely adopted in many electronic devices, including consumer electronics, laptop and battery chargers [1, 2], LED and street lighting drivers [3], and electric vehicle charging stations [4, 5, 31]. Their advantages include high power density, electrical isolation, soft-switching operation, and consequently low electromagnetic interference and harmonic emissions.

The LCC-S resonant topology introduced herein is a leading wireless counterpart to the LLC resonant converter. It is particularly suitable for EV charging applications due to its capability to handle high power levels and maintain efficiency over a range of distances and misalignment conditions [6]. Other applications include unmanned aerial vehicles [7], medical devices [8], mobile phones, and various consumer electronics [9].

This paper provides a thorough theoretical analysis of the non-wireless resonant LLC topology and the resonant LCC-S system employed in WPT. The main electrical circuits of both configurations are discussed in detail, and first harmonic appro-

ximation models of the topologies are developed, followed by their frequency-domain counterparts. Based on computational modelling using MATLAB and the LTspice electronic circuit simulator, the voltage gain characteristics over a wide frequency spectrum are presented. As demonstrated, both resonant systems are characterized by load-independent operation for switching frequencies corresponding to the resonant frequencies of the individual resonant tanks. The inductive nature of the latter ensures soft switching within the front-end square-wave generators. Such a design greatly improves the overall power conversion efficiency.

In the final section, a prototype integrated LLC resonant converter is designed and built to assess its performance over various switching frequencies. Infrared thermography is employed to map temperature distribution across critical components.

This paper primarily sought to demonstrate, via computer--based simulations, the load-independent performance at resonant points and the soft-switching behaviour of resonant circuits in both resonant topologies under investigation. Existing literature providing voltage gain characteristics across a broad frequency range for the LCC-S topology remains relatively limited. Additionally, the study explored whether precise adjustment of the switching frequency of the square-wave generator to match the resonant frequency is advantageous from a design perspective, and assessed the feasibility of implementing the LLC topology over a wide output voltage range without detrimental effects on power conversion efficiency and other key performance parameters.
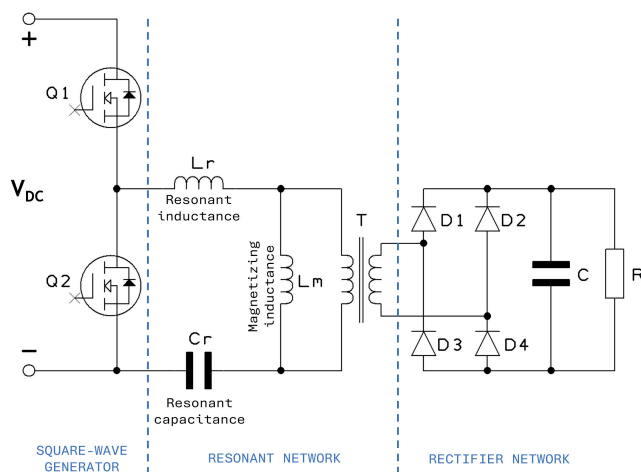
2. LLC resonant topology in non–wireless power transfer

LLC resonant converters are extensively used in numerous electronics-based applications, often emerging as the preferred solution due to their superior power conversion efficiency, high power density, high switching frequencies coupled with soft switching capabilities, and low electromagnetic emissions [14–17]. Another notable advantage of this topology is its cost--effectiveness when compared to alternative resonant converter configurations, primarily due to its reduced component count and the integration potential of magnetic components [10, 13].

The basic configuration of an LLC resonant converter, represented in Fig. 1, comprises three major circuit blocks: a square wave generator, a resonant circuit, and a rectification circuit. The square wave generator is implemented using a half-bridge topology, where switches Q1 and Q2 are alternately driven with a duty cycle of 50 % for each device, and a suitable dead time is introduced between consecutive switching transitions. That part of the converter can also be implemented as a full-bridge, an alternative to the half-bridge configuration, both having their own merits [11]. The resonant circuit of an LLC converter comprises, as its very name suggests, two inductive components, namely a resonant inductor Lr and a resonant transformer with a magnetizing inductance of L_m, and a resonant capacitor Cr. The resonant inductance L_r and the resonant capacitance C_r are finely tuned to resonate at a predetermined frequency (the switching frequency of the square wave generator), thereby ensuring that their combined impedance is effectively nullified under these conditions, Eq. 1:
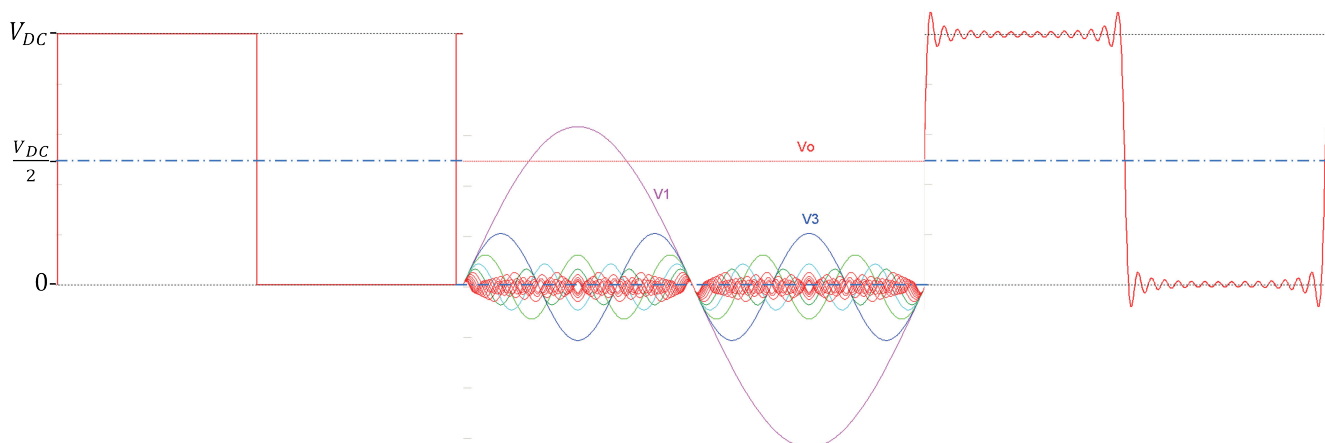
$$j \cdot \omega_r \cdot L_r - j \cdot \frac{1}{\omega_r \cdot C_r} = 0 \qquad (1)$$

where $\omega_r = 2 \cdot \pi \cdot f_r$, rad/s; f_r is the resonant frequency, Hz; j is the imaginary unit $\sqrt{-1}$.

The periodic switching waveform can be represented using a Fourier series (Fig. 2), which consists of many harmonic components of different frequencies as shown in Eq. 2.

$$V_{DCin} = \frac{V_{DC}}{2} + \frac{4 \cdot V_{DC}}{\pi \cdot 2} \cdot \sum_{n=1}^{\infty} \frac{\sin(n \cdot \omega \cdot t)}{n} \qquad (2)$$

where V_{DCin} is the square-wave generated, V; V_{DC} is the amplitude of the square-wave, V; n is the number of individual harmonics; t is time, s.

Fig. 1. Main circuits of LLC resonant converter
Rys. 1. Główne obwody przetwornicy rezonansowej typu LLC

Fig. 2. Fourier series representation of rectangular waveform. Left – square wave, middle – harmonics, right – sum of 30 harmonics
Rys. 2. Rozkład sygnału prostokątnego na szereg Fouriera. Fala prostokątna (z lewej), składowe harmoniczne (środek), suma 30 składowych harmonicznych (z prawej)

Since the resonant tank network responds only to the fundamental component of the switched square wave, the tank currents and voltages are essentially sinusoidal at the switching frequency (Eq. 3), with higher harmonics strongly attenuated by the total impedance of the resonant circuit.

$$V_{DC_1} = \frac{2 \cdot V_{DC}}{\pi} \cdot \sin(\omega \cdot t) \qquad (3)$$

where V_{DC_1} is the fundamental of the switched square wave, V.

Since the current and voltage waveforms in the primary winding of the transformer are inherently sinusoidal, the induced currents and voltages in the secondary winding preserve this sinusoidal behaviour. As can be inferred from Fig. 3, the output current I_0 constitutes the average (or DC) component of the rectified current $|I_0|$, given that the alternating component is bypassed by the capacitor whereas the direct component is retained, Eq. 4.

$$I_0 = \frac{2}{T} \cdot \int_0^{\frac{T}{2}} |I_S(t)| dt = \frac{2}{\pi} \cdot I_{S_{max}} \qquad (4)$$

where T is the period, s; $|I_S(t)|$ is the rectified secondary current, A; $I_{S_{max}}$ is the peak value of $|I_S(t)|$, A.

Hence, Eq. 5:

$$I_S = I_{S_{max}} \cdot \sin(\omega \cdot t) = \frac{\pi}{2} \cdot I_0 \cdot \sin(\omega \cdot t) \qquad (5)$$

where I_s is the current in the secondary winding of the transformer, A.

The secondary-side voltage V_S, like its primary counterpart, can be approximated by the fundamental component of its waveform, as higher harmonics do not contribute to power transfer [18]. Since the square wave at the secondary winding terminals essentially swings between $+V_0$ and $-V_0$, the fundamental harmonic can be expressed as Eq. 6:

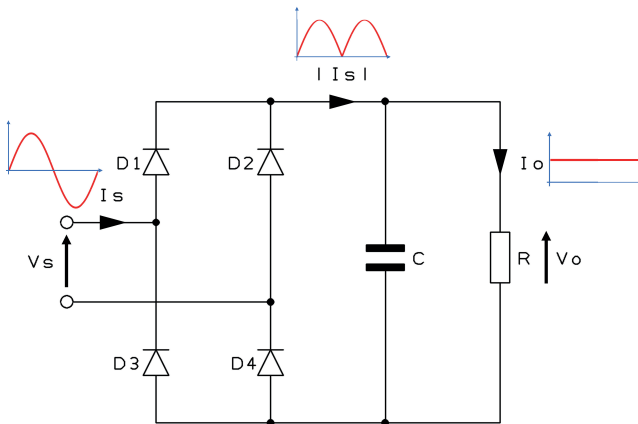$$V_{S_1} = \frac{4 \cdot V_0}{\pi} \sin(\omega \cdot t) \qquad (6)$$

where V_{S_1} is the fundamental of the secondary-side voltage V_S, V; V_0 is the output voltage, V.

Having established the current and voltage in the secondary winding, we can proceed to determine the secondary side equivalent resistance R_e, Eq. 7.

$$R_e = \frac{V_{S_1}}{I_S} = \frac{\frac{4 \cdot V_0}{\pi} \sin(\omega \cdot t)}{\frac{\pi}{2} \cdot I_0 \cdot \sin(\omega \cdot t)} = \frac{8 \cdot V_0}{\pi^2 \cdot I_0} = \frac{8}{\pi^2} \cdot R \qquad (7)$$

where R is the output resistance, Ω.

The primary-side equivalent resistance R_{ac} is obtained by multiplying the original value by the square of the transformer's turns ratio N. Hence, Eq. 8:

$$R_{ac} = R_e \cdot N^2 = \frac{8 \cdot N^2}{\pi^2} \cdot R \qquad (8)$$

The equivalent circuit corresponding to the sinusoidal approximations outlined above is portrayed in Fig. 4.

The voltage gain G of the LLC resonant converter model in Fig. 4 at the resonant frequency is given by the following formula, Eq. 9:

$$G = \frac{N \cdot V_{S_1}}{V_{DC_1}} = \frac{\frac{N \cdot 4 \cdot V_0}{\pi} \sin(\omega \cdot t)}{\frac{2 \cdot V_{DC}}{\pi} \cdot \sin(\omega \cdot t)} = 2 \cdot N \cdot \frac{V_0}{V_{DC}} \qquad (9)$$

Constructing a frequency-domain model of the circuit in Fig. 4 (Fig. 5) enables thorough evaluation of the voltage transfer function over a broad range of operating frequencies, thereby extending the analysis beyond the resonant point.
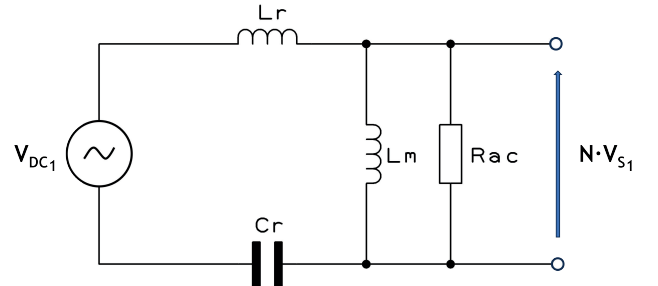

Fig. 4. First harmonic approximation model for LLC resonant converter
Rys. 4. Schemat zastępczy przetwornicy rezonansowej typu LLC dla składowej podstawowej

Fig. 3. Full-wave rectifier network and the fundamental harmonic of current waveforms in LLC resonant converter
Rys. 3. Układ dwupołówkowego układu prostowniczego z przebiegami prądu dla składowej podstawowej w przetwornicy rezonansowej typu LLC
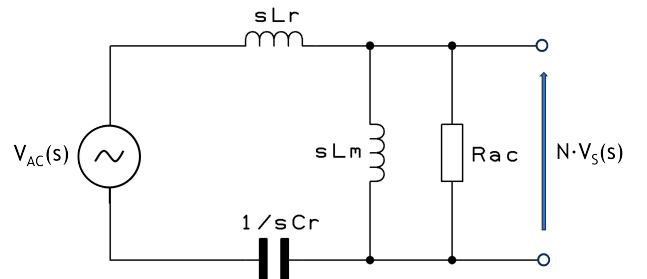

Fig. 5. Frequency-domain equivalent model of LLC converter
Rys. 5. Zastępczy model częstotliwościowy przetwornicy rezonansowej typu LLC

The transfer function of the above system is formulated as the ratio of the output voltage $V_S(s)$ to the input voltage $V_{AC}(s)$, Eq. 10:

$$H(s) = \frac{N \cdot V_S(s)}{V_{AC}(s)} \tag{10}$$

where $s = j \cdot \omega$.

Hence, Eq. 11:

$$H(s) = \frac{\dfrac{s^2}{\omega_r^2}(m-1)}{\left(\dfrac{s^2}{\omega_p^2}+1\right)+\dfrac{s}{\omega_r}\left(\dfrac{s^2}{\omega_r^2}+1\right)(m-1)Q} \tag{11}$$

where $\omega_r = \dfrac{1}{\sqrt{L_r \cdot C_r}}$; L_p is the primary-side inductance, $L_p = L_r + L_m$, H; $m = \dfrac{L_p}{L_r}$; ω_p is the resonant angular frequency for L_p and C_r, $\omega_p = \dfrac{1}{\sqrt{L_p \cdot C_p}}$; Z_0 is the characteristic impedance, $Z_0 = \sqrt{\dfrac{L_r}{C_r}}$, Ω; Q is the quality factor, $Q = \dfrac{Z_0}{R_{ac}}$.

The voltage transfer function corresponds to the absolute value of the transfer function $H(s)$, Eq. 12:

$$G = \left|H(s)\right| = \left|\frac{\dfrac{\omega^2}{\omega_r^2}(m-1)}{\left(\dfrac{\omega^2}{\omega_p^2}-1\right)+j\dfrac{\omega}{\omega_r}\left(\dfrac{\omega^2}{\omega_r^2}-1\right)(m-1)Q}\right| \tag{12}$$

This transformation enables the derivation of the complete voltage gain characteristic of the LLC resonant converter. As depicted in Fig. 6, the frequency response reveals two reso-nance points: one corresponding to the values of L_r and C_r and another to L_p and C_r. The optimal operating point of the *LLC* resonant converter is the resonant frequency determined by the $L_r - C_r$ pair. The plots are generated for various values of the converter's quality factor, Q. The most important feature of this converter is the near-complete independence of gain characteristic of the load, provided that switching occurs at or around the resonant frequency of the resonant inductor and capacitor. At this operating point, the voltage gain is equal to 1 regardless of the load variation.

The LLC converter architecture also supports integration of the resonant inductor into the transformer by exploiting the leakage inductance of the latter. This is accomplished by purposefully designing the transformer with reduced magnetic coupling. By increasing the physical separation or adjusting the winding configuration, the leakage inductance can be augmented to the desired value. As a result, the LLC resonant tank can be implemented using only the transformer and the resonant capacitor, reducing the magnetic component count. When constructing the magnetic components in the described manner, the LLC converter's circuit depicted in Fig. 1 requires modification as illustrated in Fig. 7, due to the presence of leakage inductances in both the primary and secondary side. Neglecting the secondary side leakage inductance typically results in inaccurate design parameters for the transformer [12].

The primary-side inductance L_p and the magnetizing inductance L_m are obtained by referencing the secondary-side leakage inductance to the primary side under the assumption $N^2 \cdot L_{slk} = L_{plk}$, and hence, Eq. 13:

$$L_p = L_m + L_{plk} \tag{13}$$

where L_{plk} is the primary-side leakage inductance, H.

In practical transformer design, the parameters defined by L_p and L_r (the actual resonant inductance, $L_r = L_{plk} + L_m || L_{plk}$) can be directly measured on the transformer. The measurement of L_p is conducted with the secondary winding open-circuited, while L_r is assessed with the secondary winding short-circuited. Considering the adjustments detailed above, the voltage transfer function originally given by Eq. 12 is converted into the equivalent expression shown in Eq. 14.
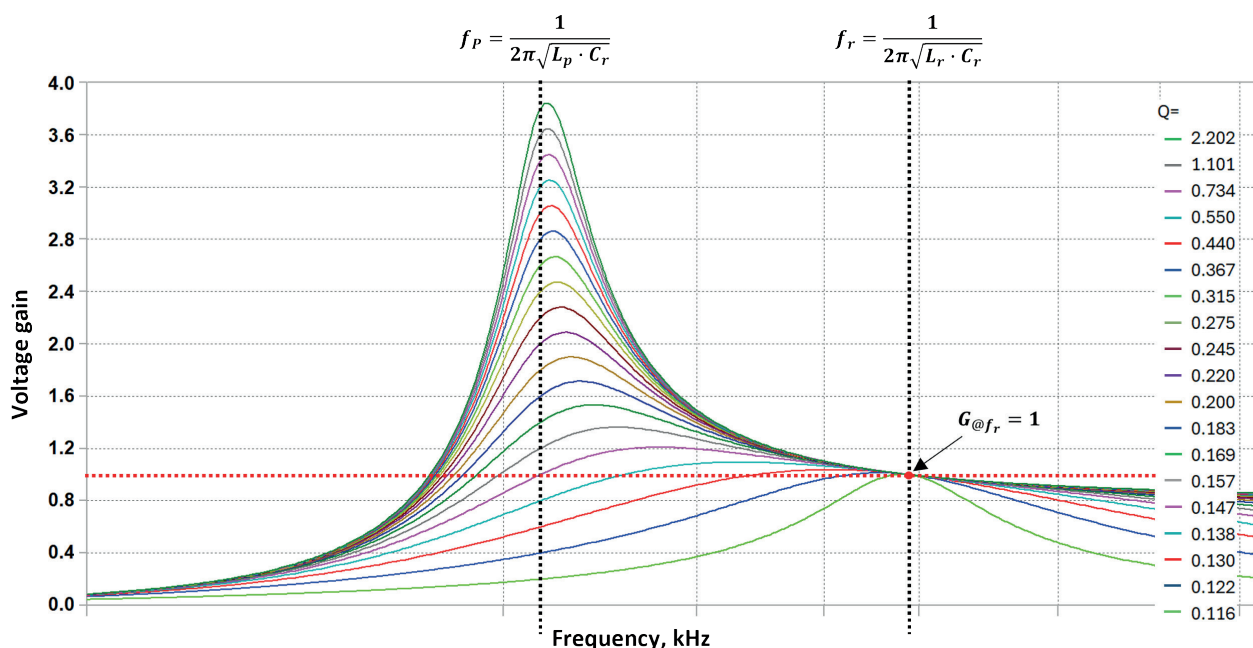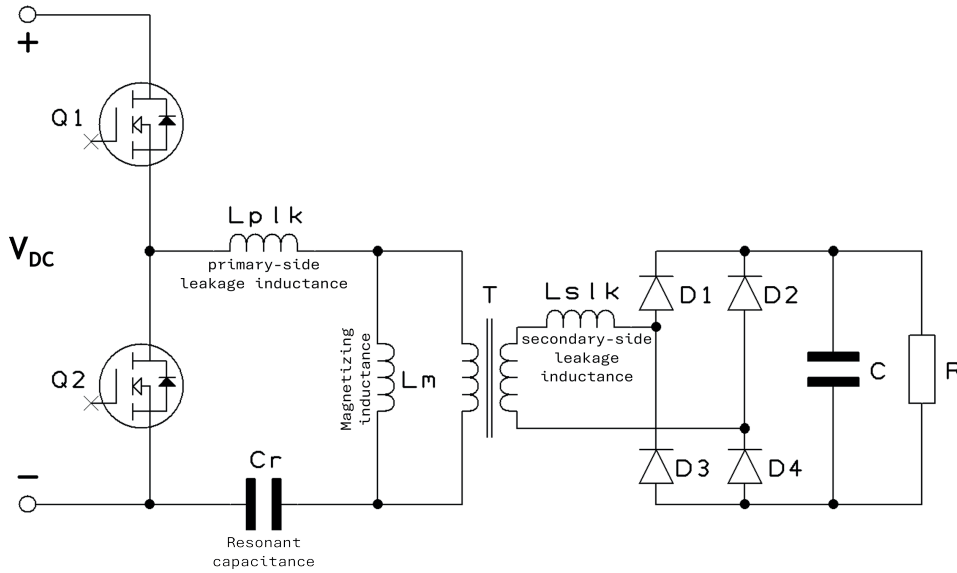

Fig. 6. Voltage gain of LLC converter for different Q values
Rys. 6. Wzmocnienie napięciowe przetwornicy rezonansowej typu LLC dla różnych wartości współczynnika Q

$$G = \left| \frac{\dfrac{\omega^2}{\omega_r^2}\sqrt{m(m-1)}}{\left(\dfrac{\omega^2}{\omega_p^2}-1\right)+j\dfrac{\omega}{\omega_r}\left(\dfrac{\omega^2}{\omega_r^2}-1\right)(m-1)Q_e} \right| \quad (14)$$

where:

$$Q_e = \frac{\sqrt{\dfrac{L_r}{C_r}}}{R_{ac_e}} \qquad R_{ac_e} = \frac{8 \cdot N^2 \cdot R}{\pi^2} \cdot \frac{m-1}{m}$$

The voltage gain at the resonant frequency ω_r or f_r, which is unity according to Eq. 12 for two isolated magnetic components, is observed to be greater than unity in the case of an integrated transformer (Fig. 8). This is a consequence of the extra gain effect caused by the leakage inductance present in the secondary side of the transformer.

The design of LLC resonant converters ensures that the operating conditions are maintained within a frequency band characterized by inductive impedance in the resonant circuit. This inductive region extends beyond the resonance peak determined by the $L_p - C_r$ pair toward higher frequencies (Fig. 9). The inductive nature induces a phase delay between the resonant current and the applied voltage waveform, such that the current reaches zero after the voltage zero-crossing event. This enables the discharge of the output capacitance of the power transistors and allows switching under zero drain-to-source voltage conditions known as ZVT, significantly reducing switching losses.

The presented resonant tank current waveforms in the LLC converter in Fig. 10 evidence that when the transistor switching frequency is tightly coupled to the resonant frequency, the resultant current is essentially sinusoidal, with localized perturbations where the transistors undergo switching transitions. Conversely, a poorly engineered resonant circuit induces significant waveform distortion with elevated harmonic components, which compromises the converter's performance and induces extra power dissipation, thus impairing the overall conversion efficiency [19].
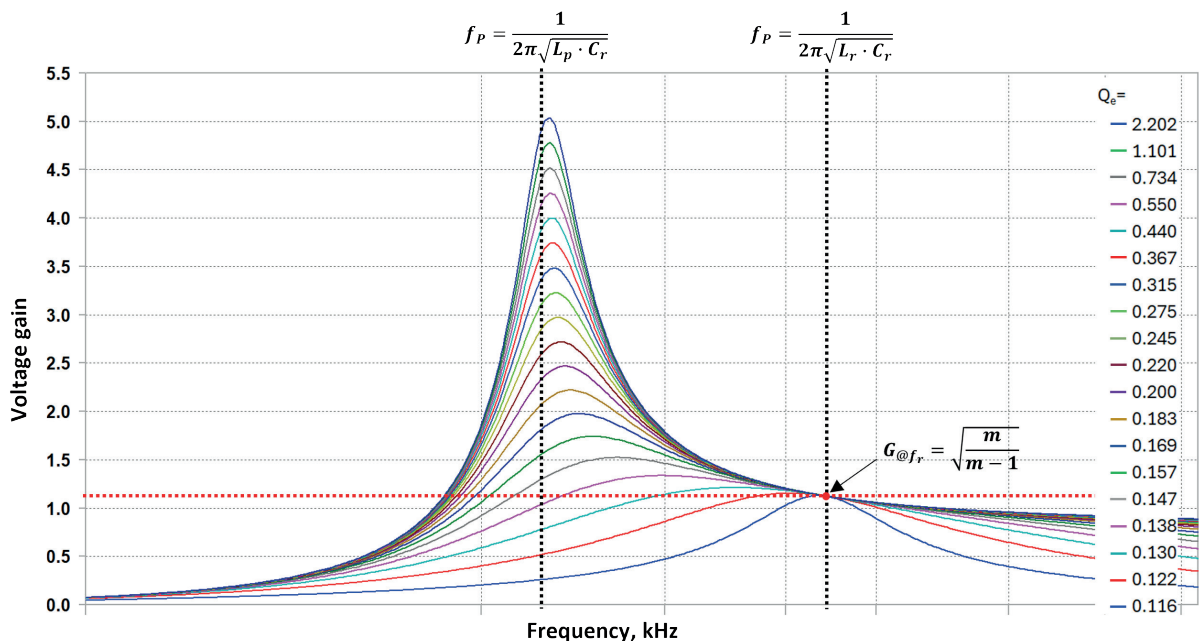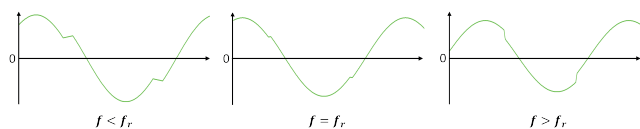

Fig. 8. Voltage gain of LLC converter with integrated transformer for different Q values
Rys. 8. Wzmocnienie napięciowe przetwornicy rezonansowej typu LLC ze zintegrowanym transformatorem dla różnych wartości współczynnika Q
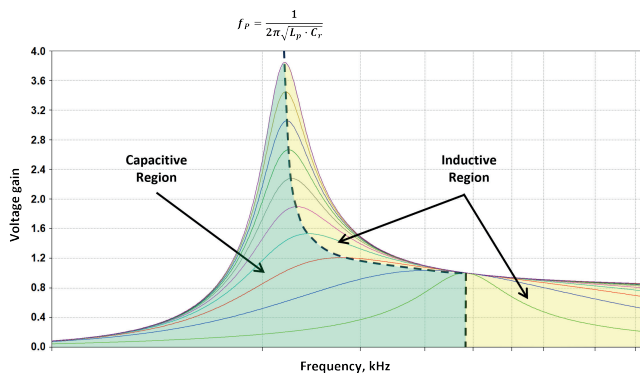
Fig. 9. Capacitive and inductive operation regions of LLC resonant converter
Rys. 9. Obszary pracy o charakterze pojemnościowym i indukcyjnym dla przetwornicy rezonansowej typu LLC

Fig. 11. Main circuits of WPT system based on LCC-S resonant converter
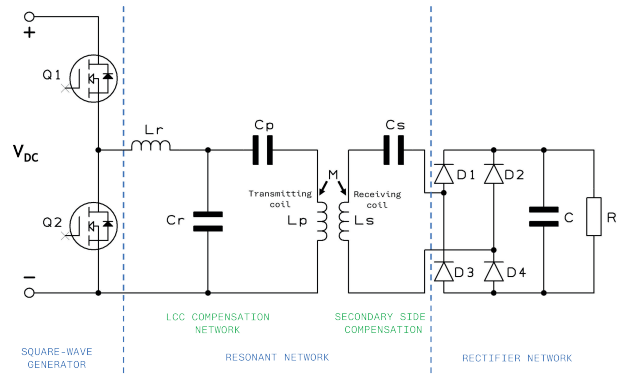Rys. 11. Główne obwody systemu WPT opartego na przetwornicy rezonansowej typu LCC-S

Fig. 10. Resonant tank current waveforms of LLC resonant converter for switching frequencies below (left), at (middle) and above resonant frequency (right)
Rys. 10. Przebiegi prądu obwodu rezonansowego przetwornicy rezonansowej typu LLC dla częstotliwości pracy poniżej (z lewej), równej (w środku) i powyżej częstotliwości rezonansowej (z prawej)

3. WPT with LCC-S resonant tank

LCC-S resonant WPT technology, unlike its non-wireless counterparts, enables the transfer of electrical power from a source to an electrical load across space, thereby eliminating the need for conventional wired connections. The LCC-S resonant circuit typically consists of an inductor-capacitor-capacitor (LCC) network on the primary (transmitter) side combined with a series (S) compensation on the secondary (receiver) side, forming a resonant tank that optimizes energy transfer through magnetic coupling (Fig. 11). According to the figure, the topology comprises three major blocks, similar to the LCC topology discussed previously: a square wave generator, a resonant circuit, and a rectification circuit with loading. The square-wave-generator section can be implemented using either a half-bridge or a full-bridge topology, where the switches (or pairs of switches in the 4-transistor configuration) are driven alternately with a 50 % duty cycle for each device or pair, and suitable dead times are maintained between individual switching transitions. The resonant network of the LCC-S converter is significantly more complex than that of the LLC resonant converter. The primary side resonant components L_r, C_r and C_p collectively form the LCC compensation network, whereas the secondary side compensation components L_S and C_S comprise the series resonant circuit. The inductors L_p and L_S correspond to the transmitting and receiving coils, respectively, representing their inherent self-inductances. These coils are magnetically coupled, characterized by a mutual inductance M. Analogous to the wired LLC configuration, all resonant network components are precisely tuned to target the fundamental frequency component of the switching waveform exclusively. The ratification stage is composed of diodes D1 through D4, a filter capacitor, and the load.

In order to simplify the analysis of the transfer characteristics of the system, the circuit schematic of the LCC-S compensated WPT system may be arranged as shown in Fig. 12.

Based on the first-harmonic-approximation principle, the secondary-side full-wave rectifier network is mathematically equivalent to a secondary-side resistance, R_{eq}, as shown by the analysis in Section 2 and Eq. 15. Voltage V_{OUT} is the fundamental component of the secondary-side voltage, measured at the input of the full-wave rectifier shown in Fig. 11.

$$R_{eq} = \frac{8}{\pi^2} \cdot R \tag{15}$$

The parameters on the secondary side can be referred to the primary side, thereby simplifying the circuit even more. The equivalent circuit, represented using the first harmonic approximation, is shown in Fig. 13 [20–23]. The secondary-side impedance Z_S (Eq. 16) is converted to the primary side by reflecting the equivalent load resistance through the mutual inductance M and frequency ω [24]. The equivalent impedance from the receiver side to the transmitter side Z_{sp} can then be calculated as follows (Eq. 17):
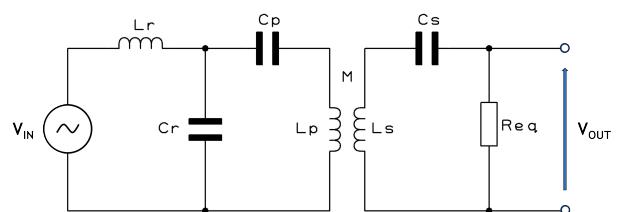
$$Z_S = R_{eq} + j\omega L_s + \frac{1}{j\omega C_s} \tag{16}$$

where L_s is the secondary-side compensation inductance, H; C_s is the secondary-side series compensation capacitance, F.

$$Z_{sp} = \frac{(\omega \cdot M)^2}{Z_S} \tag{17}$$

where M is the mutual inductance, H.

Since the series compensation capacitor C_S needs to resonate with the compensation inductor L_S at the switching (resonant) frequency, the reflected impedance can be simplified to:

Fig. 12. Simplified LCC-S compensation circuit based on first harmonic approximation
Rys. 12. Uproszczony obwód przetwornicy rezonansowej typu LCC-S dla składowej podstawowej
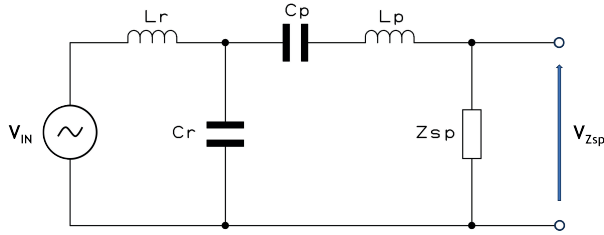
Fig. 13. Equivalent circuit of the LCC-S topology based on the first harmonic approximation
Rys. 13. Obwód zastępczy topologii LCC-S oparty na aproksymacji pierwszą harmoniczną

$$Z_{sp} = \frac{(\omega_r \cdot M)^2}{R_{eq}} \qquad (18)$$

In order to achieve the resonance of the system as a whole and hence minimise the reactive power circulating in the system, the parallel capacitance C_r must resonate with the compensation inductance L_r located on the same side. Moreover, the series compensation capacitance C_p, the parallel compensation capacitance C_r, and the transmitting coil inductance L_p collectively create a resonance, ensuring that all parameters meet the following conditions (Eq. 19, Eq. 20, Eq. 21):

$$j \cdot \omega_r \cdot L_r - j \cdot \frac{1}{\omega_r \cdot C_r} = 0 \qquad (19)$$

$$j \cdot \omega_r \cdot L_s - j \cdot \frac{1}{\omega_r \cdot C_s} = 0 \qquad (20)$$

$$j \cdot \omega_r \cdot L_p - j \cdot \frac{1}{\omega_r \cdot C_r} - j \cdot \frac{1}{\omega_r \cdot C_p} = 0 \qquad (21)$$

It can be shown [23] that the voltage gain relating the output in Fig. 12 to the voltage across Z_{sp} is given by Eq. 22:

$$\left| \frac{V_{OUT}}{V_{Zsp}} \right| = \frac{R_{eq}}{\omega_r \cdot M} \qquad (22)$$

where V_{OUT} is the output voltage as shown in Fig. 12, V; V_{Zsp} is the voltage across the reflected impedance Z_{sp} (Fig. 13), V.

Two-port network theory [25, 26] offers a convenient tool for computing the voltage gain between the input and the output $\left| \frac{V_{Zsp}}{V_{IN}} \right|$ in the system presented in Fig. 13. From the analysis, the formula shown in Eq. 23 is derived.

$$\left| \frac{V_{Zsp}}{V_{IN}} \right| = \frac{\omega_r \cdot M^2}{R_{eq} \cdot L_r} \qquad (23)$$

where V_{IN} is the fundamental of the switched square wave (the input voltage as shown in Fig. 13), V.

Finally, the voltage gain between the input and output of the LCC-S resonant converter, shown in Fig. 12 operating at the resonant frequency ω_r, can be summarized as follows (Eq. 24):

$$G = \left| \frac{V_{OUT}}{V_{IN}} \right| = \left| \frac{V_{Zsp}}{V_{IN}} \right| \left| \frac{V_{OUT}}{V_{Zsp}} \right| = \frac{\omega_r \cdot M^2}{R_{eq} \cdot L_r} \cdot \frac{R_{eq}}{\omega_r \cdot M} = \frac{M}{L_r} \qquad (24)$$

A primary advantage of this topology, as in the case of the LLC converter, is that the gain characteristics remain almost entirely unaffected by the load, as long as switching takes place at the system's resonant frequency. Under these conditions, the voltage gain, expressed in Eq. 24, is determined by the ratio of the mutual inductance M to the compensated inductor L_r, independent of load variations.

The analysis of the LCC-S resonant WPT system outlined here, along with the specified resonant conditions for the parameters of the resonant tank's components (Eq. 19, Eq. 20, Eq. 21), was employed in LTspice-based computer modelling to verify the constant voltage characteristics of the LCC-S topology and its load-independent behaviour. The simulation parameters of the system, corresponding to the circuit schematic illustrated in Fig. 11, are listed in Tab. 1.

Fig. 14 and Fig. 15 respectively depict the input and output voltage waveforms and the current waveforms of the primary and secondary coils obtained from simulations of the LCC-S system parameters specified above. It can be observed that, as long as the resonant conditions at the operating frequency are preserved, the voltage gain between the input and output of the LCC-S resonant converter can be approximated by Eq. 24 (see Eq. 25).

$$G = \left| \frac{V_{OUT}}{V_{IN}} \right| = \frac{\frac{4 \cdot V_{outDC}}{\pi}}{\frac{2 \cdot V_{inDC}}{\pi}} = \frac{2 \cdot V_{outDC}}{V_{inDC}} = 0.96 \cong \frac{M}{L_r} = 1 \qquad (25)$$

The failure to align the switching frequency of the square-wave generator with the resonant frequency of the entire LCCS system leads to the loss of a fundamental characteristic of the LCC-S topology: a constant voltage output tied to the ratio shown in Eq. 24. Such a failure also leads to the loss of another critical advantage over other types of resonant tanks: the almost complete immunity of the output voltage to load fluctuations.
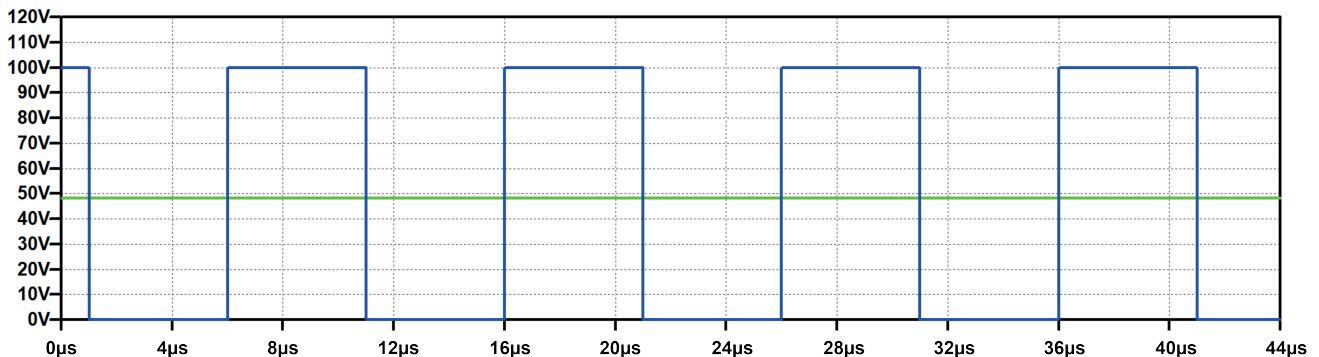

Fig. 14. Input voltage waveform (blue) and output voltage waveform (green) for LCC-S WPT system simulation parameters in Tab. 1
Rys. 14. Przebieg napięcia wejściowego (niebieski) oraz przebieg napięcia wyjściowego (zielony) dla parametrów symulacji systemu LCC-S WPT podanych w Tab. 1
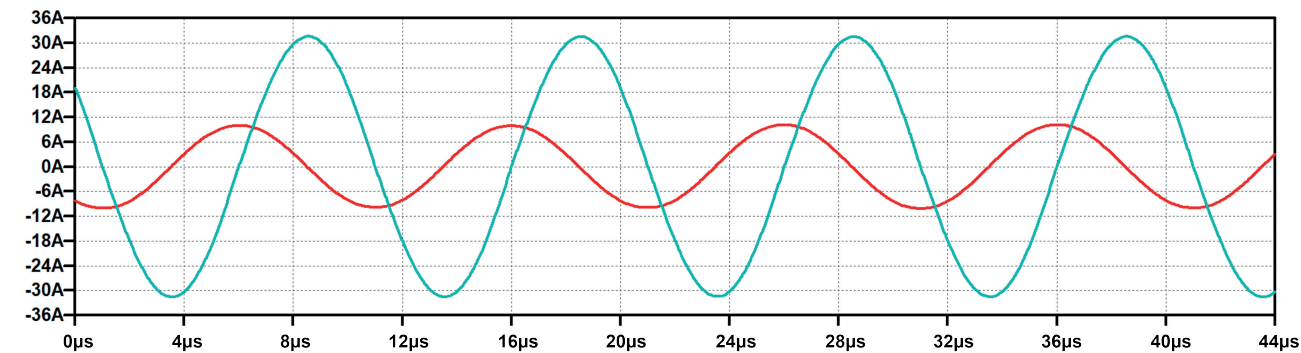
Fig. 15. Transmitting coil current waveform (red) and receiving coil current waveform (teal) for LCC-S WPT system simulation parameters in Tab. 1
Rys. 15. Przebieg prądu cewki nadawczej (czerwony) oraz przebieg prądu cewki odbiorczej (zielononiebieski) dla parametrów symulacji systemu LCC-S WPT podanych w Tab. 1
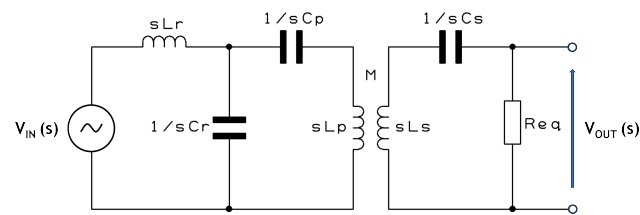

Fig.16. Frequency-domain equivalent model of LCC-S resonant WPT converter
Rys. 16. Zastępczy model częstotliwościowy przetwornicy rezonansowej bezprzewodowej typu LCC-S

For the purpose of assessing the impact of transistor switching frequency in the generator on the voltage gain response of the LCC-S WPT system, a frequency-domain circuit model based on Fig. 13 was developed (refer to Fig. 16). This modelling strategy, analogous to the one employed in LLC non-wireless resonant topology, allows for a detailed evaluation of the voltage transfer function across a wide frequency range, thus extending the scope of analysis beyond the fundamental harmonic.

Figure 17 depicts the complete voltage gain profile of the LCC-S WPT resonant converter. The plots were generated for varying values of the secondary-side resistance R_{eq}. As demon-
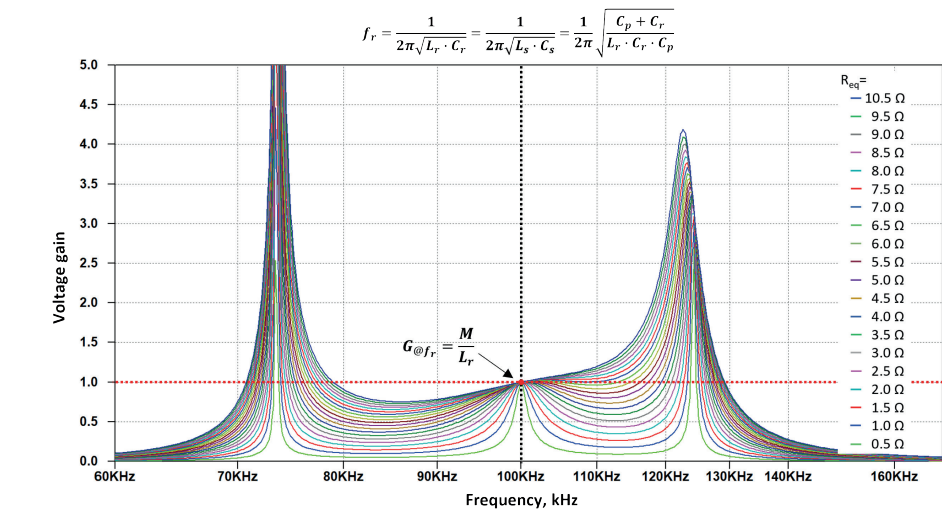
$$f_r = \frac{1}{2\pi\sqrt{L_r \cdot C_r}} = \frac{1}{2\pi\sqrt{L_s \cdot C_s}} = \frac{1}{2\pi}\sqrt{\frac{C_p + C_r}{L_r \cdot C_r \cdot C_p}}$$

Fig. 17. Voltage gain of LCC-S converter for different Req values
Rys. 17. Wzmocnienie napięciowe przetwornicy rezonansowej typu LCC-S dla różnych wartości rezystancji zastępczej Req
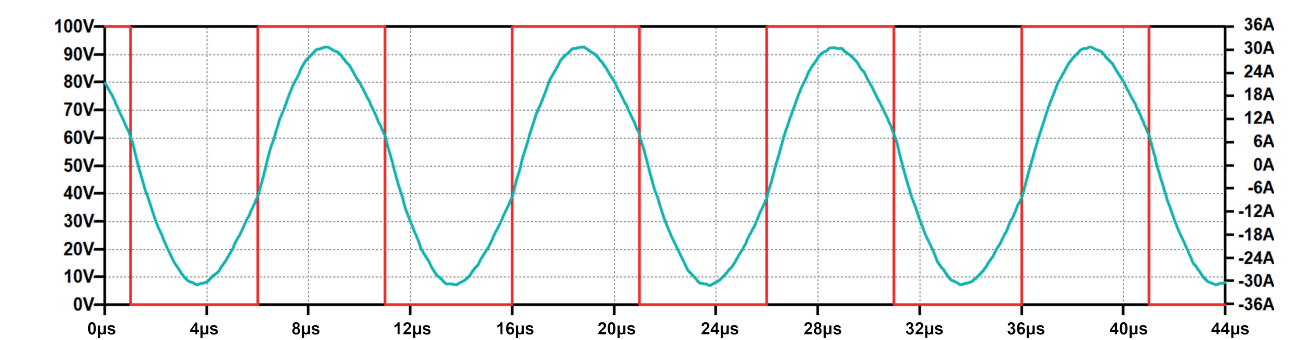

Fig. 18. Square-wave input voltage waveform (red) and transistor current waveform (teal) for LCC-S WPT system simulation parameters in Tab. 1
Rys. 18. Prostokątny przebieg napięcia wejściowego (czerwony) oraz przebiegi prądu przez tranzystory (zielononiebieski) dla parametrów symulacji systemu LCC-S WPT podanych w Tab. 1

Tab. 1. LCC-S WPT system simulation parameters
Tab. 1. Parametry symulacji bezprzewodowego systemu przesyłania mocy (WPT) typu LCC-S

Symbol	Parameter	Value
V_{inDC}	DC input voltage to square-wave generator	100 V
V_{outDC}	DC output voltage	48 V
R	Load resistance	2.4 Ω
C	Output capacitance	100 µF
f	Operating frequency	100 kHz
L_p	Primary coil inductance	50 µH
L_s	Secondary coil inductance	50 µH
L_r	Primary-side series compensation inductance	10 µH
C_p	Primary-side series compensation capacitance	63.32 nF
C_r	Primary-side parallel compensation capacitance	253.3 nF
C_s	Secondary-side series compensation capacitance	50.66 nF
M	Mutual inductance	10 µH
k	Coupling coefficient	0.2

strated, the optimal operating point of the resonant circuit aligns with the resonant frequency defined by the criteria outlined in Eq. 19, 20, and 21. When these conditions are satisfied, the gain characteristics exhibit invariance to load changes. At this frequency, the voltage gain is determined by the ratio of the mutual inductance M to the compensated inductor L_r (Eq. 24). When the switching frequency of the square-wave generator deviates from the resonant frequency ω_r, the voltage gain between the input and output terminals of the LCC-S system in Fig. 16 no longer correlates closely with the ratio of the load-side output voltage to the resonant circuit input voltage.

In practical applications, to mitigate switching losses in power transistors and improve the overall power conversion efficiency of the LCC-S WPT system, achieving the ZVT condition is desirable. The primary-side compensation components must be carefully optimized and adjusted to possess a slightly inductive character, thereby facilitating soft switching within the front-end half-bridge/full-bridge stage of the converter. Under these conditions, the fundamental harmonic of the square-wave input voltage leads the current through the transistors, indicating an inductive equivalent load for the generator section. As depicted in Fig. 18, these conditions are satisfied for the simulation parameters presented in Tab. 1.

Fig. 19. Measurement setup for thermal and performance evaluation of LLC resonant converter
Rys. 19. Układ pomiarowy do badania parametrów termicznych i elektrycznych przetwornicy impulsowej typu LLC

4. Practical Implementation of Integrated LLC Resonant Topology

To evaluate the performance of an integrated LLC resonant topology in a practical setup (Fig. 19) across various switching frequencies of the square-wave generator, and to examine its impact on the efficiency of power conversion and thermal behaviour of the converter, the LLC converter depicted in Fig. 20 was designed and constructed. The design featured the TEA19161T/2 digital controller IC [27], designed to cooperate with the TEA19162T power factor control (PFC) controller, which was also part of the design. The converter was supplied by a 230 V AC power source, with the PFC stage output voltage setpoint fixed at 400 V, which serves as the DC input
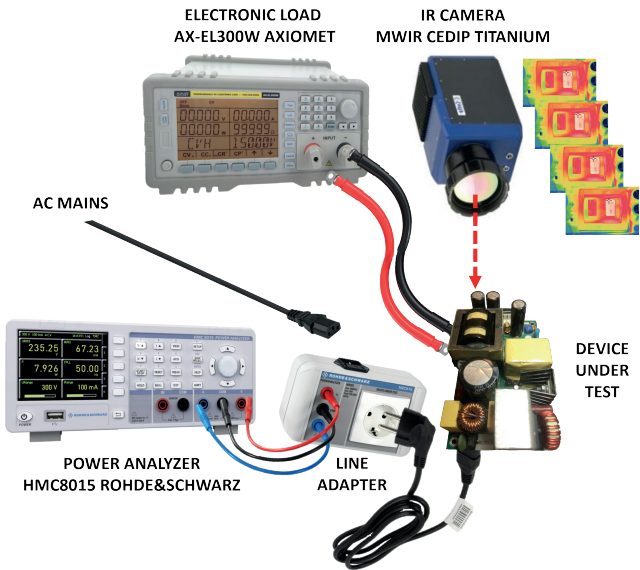
voltage to the square-wave voltage generator. Subsequently, the 400 V DC rail was applied across the resonant tank via a dual-switch half-bridge configuration. The resonant network included an integrated transformer, where the inductance ratio between the primary winding and the leakage (resonant) inductance was defined as $m = \dfrac{L_p}{L_r} = \dfrac{600\,\mu H}{150\,\mu H} = 4$.

The leakage inductance was finely tuned to resonate with a 33 nF resonant capacitor at a frequency of approximately 71 kHz. The integrated LLC resonant transformer itself (refer to Fig. 20) comprised a 47-turn primary coil of a multi-strand litz-type wire, where a carefully arranged pattern causes the current in the coil to be distributed homogenously throughout

INTEGRATED LLC RESONANT TRANSFORMER

Fig. 20. Constructed integrated LLC resonant converter
Rys. 20. Skonstruowana zintegrowana rezonansowa przetwornica impulsowa typu LLC

the strands so that the net current in each is effectively the same [28]. The secondary-side winding of the transformer was implemented in a double-tapped configuration, incorporating an intermediate terminal that effectively divided the winding into two equal segments. Each section consisted of a 5-turn coil fabricated from multi-strand litz wire with a substantially larger diameter than its primary-side counterpart to minimize effective DC resistance. These segments were simultaneously wound in meticulously designed patterns to maintain symmetrical contributions to the leakage inductance as observed from the primary side. The coils were mounted on an EER-39/45-H-9P split bobbin to meet the design criteria for resonant/leakage inductance. The overall transformer design – including wire selection, strand diameter, and strand count per bundle – followed the methodology delineated in [29], suitably adapted for the purposes of this research. The output voltage at the user end was initially regulated at 24 V, a voltage level to which the resonant tank was precisely calibrated.

To investigate the impact of the mismatch between the switching frequency of the power transistors in the square-wave generator and the resonant frequency – determined by the resonant tank's inductive and capacitive elements – on the resonant current waveforms, the output voltage delivered to the end-user was varied incrementally from 21 V to 27 V in 3 V steps. Since the LLC converter's voltage gain is directly linked to the ratio of the load-side output voltage and the PFC stage output voltage, variations in the former altered the converter's operating frequency and consequently distorted the resonant tank current waveforms (refer to Fig. 21) as anticipated based on the simulation results illustrated in Fig. 10. One can notice that
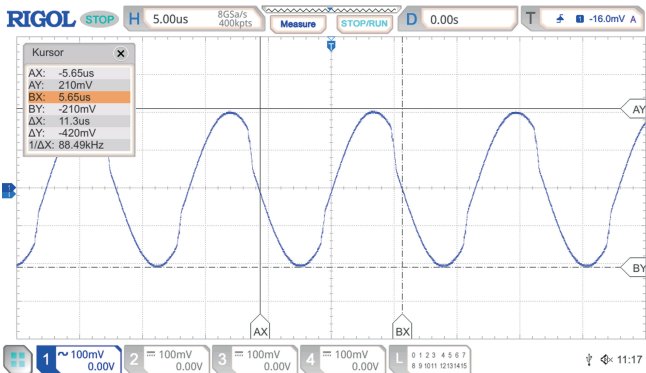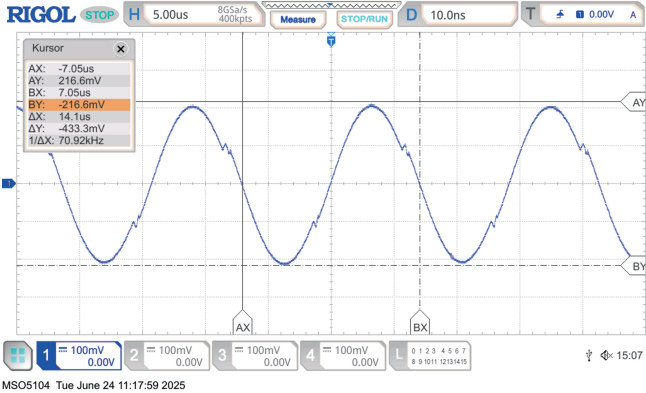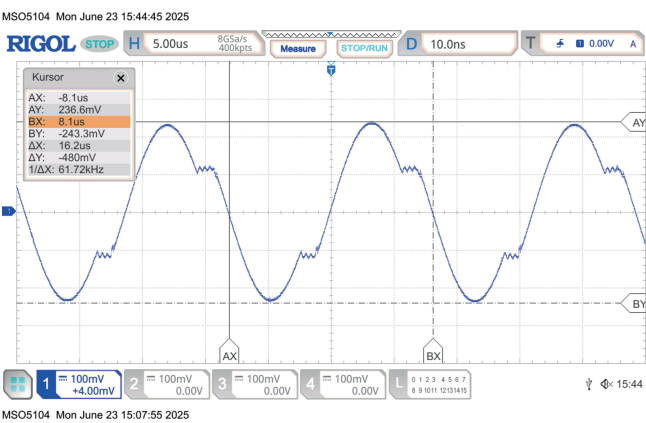
Fig. 21. Registered resonant tank current waveforms of constructed LLC resonant converter for switching frequencies below (top), at (middle) and above resonant frequency (bottom)
Rys. 21. Zarejestrowane przebiegi prądu w rezonansowym obwodzie skonstruowanej przetwornicy typu LLC dla częstotliwości pracy poniżej (góra), w (środek) oraz powyżej częstotliwości rezonansowej (dół)
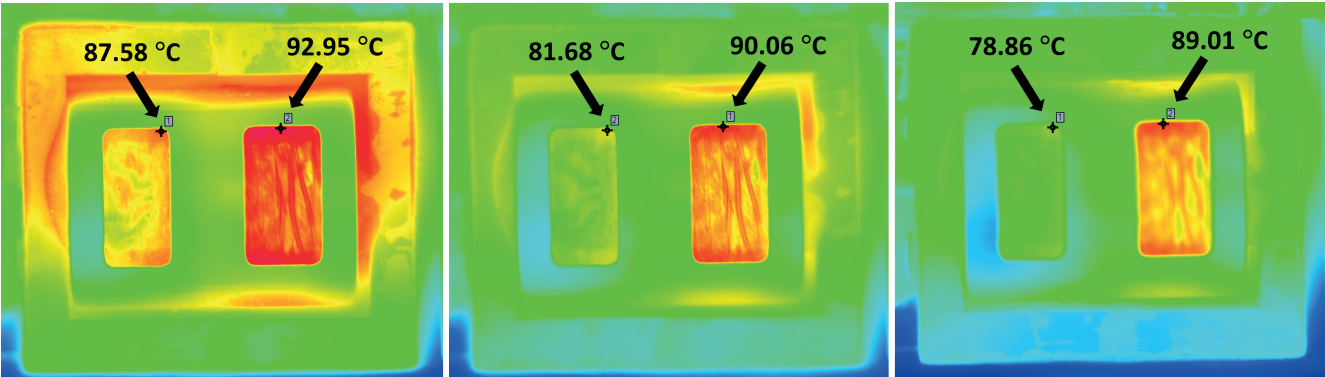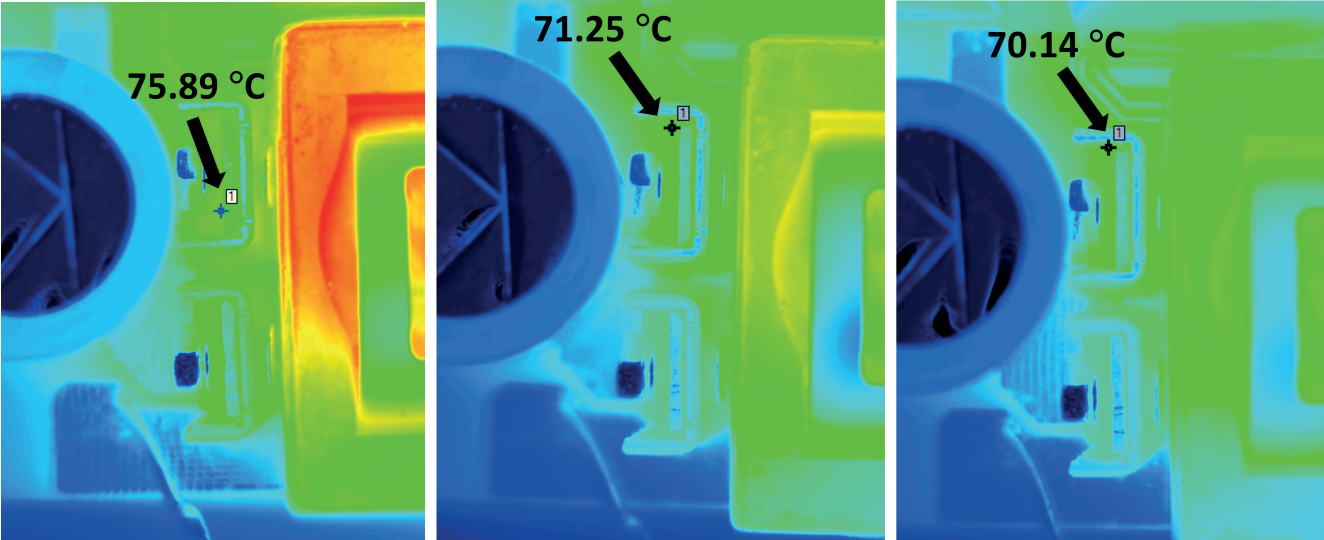

Fig. 22. Thermal images of integrated LLC resonant transformer operating below (left), at (middle) and above resonant frequency (right)
Rys. 22. Termogramy zintegrowanego rezonansowego transformatora LLC pracującego poniżej (z lewej), w (w środku) oraz powyżej częstotliwości rezonansowej (z prawej)

Fig. 23. Thermal images of transistors in square-wave generator operating below (left), at (middle) and above resonant frequency (right)
Rys. 23. Termogramy tranzystorów generatora fali prostokątnej pracujące poniżej (po lewej), w (w środku) oraz powyżej częstotliwości rezonansowej (po prawej)

the investigated output voltage setpoints yielded three distinct switching frequencies – 61.7 kHz, 71 kHz, and 88.5 kHz – in the square-wave generator section, corresponding to output voltages of 21 V (above-resonant frequency operation), 24 V (resonant frequency operation), and 27 V (below-resonant frequency operation), respectively.

Thermographic evaluation of the constructed LLC resonant converter was conducted using a MWIR Cedip Titanium cooled photon camera to determine the temperature distribution across key components, including the power transistors implemented in the square-wave generator section and the integrated LLC resonant transformer. Infrared thermography is commonly employed in power electronics, particularly for assessing temperature distribution across large areas [30]. The thermal performance of these components was expected to be most sensitive to changes in the switching frequency of the square-wave generator. Prior to the measurements, the power converter was continuously run at 250 W for each of the investigated switching frequencies, allowing the system to reach thermally steady-state conditions. Following this, a sequence of thermographic images representing the square-wave generator and the integrated magnetic component was captured, and the overall efficiency of power conversion of the LLC resonant converter was evaluated. Figure 22 illustrates the temperature distribution along the integrated LLC resonant transformer for the aforementioned frequency setpoints.

As can be noticed, both the primary (on the left side of the transformer in Fig. 22) and secondary windings, as well as the magnetic core of the resonant transformer, show the highest operating temperatures for switching frequencies below the resonant point. This is especially pronounced for the primary coil, where the discrepancy in registered temperatures for the investigated switching frequencies ranges from 6 to 9 degrees centigrade. It can be concluded that this change is largely driven by the resonant tank currents shown in Fig. 21 as they flow through the primary winding.

It is surprising that the operating temperature of the secondary coil for the region of operation below resonant frequency is the highest, since the intuitive assumption would be that power dissipation should be reduced for the lowest output currents associated with the output voltage of 27 V.

The power transistors in the square-wave generator are also placed in the path of the currents flowing through the resonant network. As expected, the maximum operating temperature was recorded for switching frequencies below the resonant point (Fig. 23). However, the steady-state temperatures of the power switches are largely comparable, and their operation remains well within the inductive region, despite significant swings in switching frequency.

The above observations are consistent with the recorded power conversion efficiency for all three setpoints. The lowest efficiency of 91.47 % was measured for below-resonant operation, whereas the highest efficiency (91.55 %) was observed at the switching frequency corresponding to the resonant point. Operation above the resonant frequency yielded an efficiency of about 91.54 %.

5. Conclusion

This research focuses on two prominent resonant topologies used in switch-mode power supplies: one conventional, non-wireless design with an LLC resonant circuit, and another used in WPT systems featuring an LCC-S resonant tank. The paper presents a detailed theoretical discussion of both resonant networks, outlining their operating principles and assessing their respective advantages and limitations. Using first harmonic approximation models, the fundamental relationships between the input and output voltages of these topologies are demonstrated. The study illustrates two significant advantages of these resonant topologies – load-independent operation at resonance and zero-voltage switching across the full operating range for inductive circuits – by constructing frequency-domain models and plotting voltage gain characteristics over a wide frequency spectrum. The latter is not well explored in the current body of literature, especially regarding the LCC-S resonant topology. The study also explores how discrepancies between the switching frequency of the square-wave generator's power transistors and the resonant frequency affect current and voltage waveforms in the resonant tanks. Finally, a prototype integrated LLC resonant converter was designed and constructed to test its efficiency and thermal performance over an extended switching frequency range. This was done in order to investigate whether fine-tuning the switching frequency of the square-wave generator to align with the resonant frequency offers benefits from a design standpoint, and to assess the capability of the LLC topology to operate effectively across a wide range of output voltages without causing adverse effects on power conversion efficiency and other key

performance criteria. As demonstrated, the power conversion efficiency measured at the tested setpoints was only minimally affected by operating frequencies outside the resonant point, primarily because the operation stayed well within the inductive region of the resonant tank.

Acknowledgments

References

1. Kim B.-C., Park K.-B., Kim C.-E., Lee B.-H., Moon G.-W., *LLC Resonant Converter With Adaptive Link-Voltage Variation for a High-Power-Density Adapter*, "IEEE Transactions on Power Electronics", Vol. 25, No. 9, 2010, 2248–2252, DOI: 10.1109/TPEL.2010.2050906.

2. Dow Y.S., Son H.I., Lee H.-D., *A Study on Half Bridge LLC Resonant Converter for Battery Charger on Board*, [In:] 8th International Conference on Power Electronics – ECCE Asia, Jeju, South Korea, 2011, DOI: 10.1109/ICPE.2011.5944758.

3. Bas Y., Akboy E., *A High-Efficiency LLC Resonant Converter For LED Driver Applications*, [In:] 7th International Congress on Human-Computer Interaction, Optimizing and Robotic Applications (ICHORA), Ankara, Turkiye, 2025, DOI: 10.1109/ICHORA65333.2025.11017094.

4. Deng J.J., Li S., Hu S., Mi C.C., Ma R.-Q., *Design Methodology of LLC Resonant Converters for Electric Vehicle Battery Chargers*, "IEEE Transactions on Vehicular Technology", Vol. 63, No. 4, 2014, 1581–1592, DOI: 10.1109/TVT.2013.2287379.

5. Pandey R., Singh B., *A Power-Factor-Corrected LLC Resonant Converter for Electric Vehicle Charger Using Cuk Converter*, "IEEE Transactions on Industry Applications", Vol. 55, No. 6, 2019, 6278–6286, DOI: 10.1109/TIA.2019.2934059.

6. Wang W.B., Deng J.J., Chen D.L., *An LCC-S compensated wireless power transfer system using receiver-side switched-controlled capacitor combined semi-active rectifier for constant voltage charging with misalignment tolerance*, "IET Power Electronics", Vol. 16, No. 7, 2023, 1103–1114, DOI: 10.1049/pel2.12453.

7. Wu S., Cai C., Liu X., Chai W., Yang S., *Compact and Free-Positioning Omnidirectional Wireless Power Transfer System for Unmanned Aerial Vehicle Charging Applications*, "IEEE Transactions on Power Electronics", Vol. 37, No. 8, 2022, 8790–8794, DOI: 10.1109/TPEL.2022.3158610.

8. Xiao C., Cheng D., Wei K., *An LCC-C Compensated Wireless Charging System for Implantable Cardiac Pacemakers: Theory, Experiment, and Safety Evaluation*, "IEEE Transactions on Power Electronics", Vol. 33, No. 6, 2018, 4894–4905, DOI: 10.1109/TPEL.2017.2735441.

9. Xu W., Liang W., Peng J., Liu Y., Wang Y., *Maximizing Charging Satisfaction of Smartphone Users via Wireless Energy Transfer*, "IEEE Transactions on Mobile Computing", Vol. 16, No. 4, 2016, 990–1004, DOI: 10.1109/TMC.2016.2577585.

10. Korobok M.A., Shemolin I.S., Sazykin K.B., *Practical Implementation of an LLC Converter with Integrated Resonant Circuit Elements*, [In:] International Russian Smart Industry Conference (SmartIndustryCon), Sochi, Russian Federation, 2024, DOI: 10.1109/SmartIndustryCon61328.2024.10515714.

11. Zeng J.M., Zhang G.D., Yu S.S., Zhang B., Zhang Y., *LLC resonant converter topologies and industrial applications – A review*, "Chinese Journal of Electrical Engineering", Vol. 6, No. 3, 2020, 73–84, DOI: 10.23919/CJEE.2020.000021.

12. Fairchild Semiconductor Corporation, Application Note AN-4151, Half-Bridge LLC Resonant Converter Design Using FSFR-Series Fairchild Power Switch (FPS™), Rev. 1.0.2, Oct−2014.

13. Gao S.W., Zhao Z.Y., *Magnetic Integrated LLC Resonant Converter Based on Independent Inductance Winding*, "IEEE Access", Vol. 9, 2020, 660–672, DOI: 10.1109/ACCESS.2020.3046616.

14. Saket M.A., Shafiei N., Ordonez M., *LLC Converters With Planar Transformers: Issues and Mitigation*, "IEEE Transactions on Power Electronics", Vol. 32, No. 6, 2020, 4524–4542, DOI: 10.1109/TPEL.2016.2602360.

15. Fei C., Lee F. C., Li Q., *High-Efficiency High-Power-Density LLC Converter With an Integrated Planar Matrix Transformer for High-Output Current Applications*, "IEEE Transactions on Industrial Electronics", Vol. 64, No. 11, 2017, 9072–9082, DOI: 10.1109/TIE.2017.2674599.

16. Sun S.Z., Fu J.Q., Wei L.S., *Optimization of High-Efficiency Half-bridge LLC Resonant Converter*, [In:] 2021 40th Chinese Control Conference (CCC), Shanghai, China, DOI: 10.23919/CCC52363.2021.9550087.

17. Luo J.H., Wang J.H., Fang Z.J., Shao J.W., Li J.G., *Optimal Design of a High Efficiency LLC Resonant Converter with a Narrow Frequency Range for Voltage Regulation*, "Energies", Vol. 11, No. 5, 2018, DOI: 10.3390/en11051124.

18. Erickson R.W., Maksimović D., *Fundamentals of Power Electronics*, Springer International Publishing, 2020, ISBN: 9783030438791.

19. Cetin S., Yenil V., *Optimal Operation Region of LLC Resonant Converter for on-Board EV Battery Charger Applications*, [In:] 2018 IEEE 18th International Power Electronics and Motion Control Conference (PEMC), Budapest, Hungary, DOI: 10.1109/EPEPEMC.2018.8521857.

20. Zhao R., Xu F., *Design of Wireless Power Transfer System Based on LCC-S*, "Journal of Physics: Conference Series", Vol. 2496, 2023, DOI: 10.1088/1742-6596/2496/1/012014.

21. Solimene L., Corti F., Musumeci S., Reatti A., Ragusa C.S., *A controlled variable inductor for an LCC-S compensated Wireless Power Transfer system*, [In:] IECON 2022 – 48th Annual Conference of the IEEE Industrial Electronics Society, Brussels, Belgium (2022), DOI: 10.1109/IECON49645.2022.9968576.

22. Yang J.F., Zhang X.D., Zhang K.J., Cui X.Y., Jiao C.Q., Yang X., *Design of LCC-S Compensation Topology and Optimization of Misalignment Tolerance for Inductive Power Transfer*, "IEEE Access", Vol. 8, 2020, 191309–191318, DOI: 10.1109/ACCESS.2020.3032563.

23. Geng Y., Li B., Yang Z., Lin F., Sun H., *A High Efficiency Charging Strategy for a Supercapacitor Using a Wireless Power Transfer System Based on Inductor/Capacitor/Capacitor (LCC) Compensation Topology*, "Energies", Vol. 10, No. 1, 2017, DOI: 10.3390/en10010135.

24. Wang C.S., Covic G.A., Stielau O.H., *Power transfer capability and bifurcation phenomena of loosely coupled inductive power transfer systems*, "IEEE Transactions on Industrial Electronics", Vol. 51, No. 1, 2004, 148–157, DOI: 10.1109/TIE.2003.822038.

25. Li S.Q., Mi C.C., *Wireless Power Transfer for Electric Vehicle Applications*, "IEEE Journal of Emerging and

Selected Topics in Power Electronics", Vol. 3, No. 1, 2015, 4–17, DOI: 10.1109/JESTPE.2014.2319453.

26. Orfanidis S.J., *Electromagnetic Waves and Antennas*, Rutgers University, 2016, [https://rutgers.app.box.com/s/rwzi-fofsu9slf8xy38f6uwhjd5gmn2q7].

27. NXP Semiconductors, *Digital controller for high-efficiency resonant power supply*, Rev. 2.2 – 23 January 2023, [www.nxp.com/docs/en/data-sheet/TEA19161T.pdf].

28. Sullivan C.R., *Optimal choice for number of strands in a litz-wire transformer winding*, "IEEE Transactions on Power Electronics", Vol. 14, No. 2, 1999, 283–291, DOI: 10.1109/63.750181.

29. Sullivan C.R., Zhang R.Y., *Simplified Design Method for Litz Wire*, [In:] 2014 IEEE Applied Power Electronics Conference and Exposition – APEC 2014, Fort Worth, TX, USA (2014), DOI: 10.1109/APEC.2014.6803681.

30. Barlik R., Nowak M., Grzejszczak P., Zdanowski M., *Estimation of power losses in a high-frequency planar transformer using a thermal camera*, "Archives of Electrical Engineering", Vol. 65, No. 3, 2016, 613–627, DOI: 10.1515/aee-2016-0044.

31. Detka K., Górecki K., *Wireless Power Transfer – A Review*, "Energies", Vol. 15, No. 19, 2022, DOI: 10.3390/en15197236.

Wybrane topologie rezonansowe dla przewodowego i bezprzewodowego systemu przesyłania energii

Streszczenie: Topologie rezonansowe przetwornic impulsowych są szeroko stosowane w różnych sektorach przemysłu elektronicznego ze względu na ich istotne zalety, takie jak wysoka sprawność, duża gęstość mocy, izolacja galwaniczna, niskie zakłócenia elektromagnetyczne (EMI) i zniekształcenia harmoniczne, możliwość integracji magnetycznej, przełączanie kluczy elektronicznych przy zerowym napięciu oraz praca przy wysokich częstotliwościach. W niniejszym artykule przedstawiono dwie główne konfiguracje obwodów rezonansowych: topologię typu LLC z konwencjonalnym transformatorem oraz topologię LCC-S dla bezprzewodowego systemu przesyłania energii (WPT). Druga z nich wykorzystuje sprzężenie magnetyczne do przesyłu energii na odległość, eliminując tym samym zależność od tradycyjnych rozwiązań transformatorowych. Przedstawiono również szczegółowy opis teoretyczny obu obwodów rezonansowych wraz z analizą ich zalet i wad. Wykazano, że obie topologie osiągają wysoką sprawność przetwarzania mocy dzięki przełączaniu tranzystorów mocy w momencie, gdy napięcie na nich jest bliskie zeru (ZVT). Ponadto topologie te gwarantują istotną przewagę nad innymi rozwiązaniami rezonansowymi ze względu na niezależność napięcia wyjściowego od zmian obciążenia, pod warunkiem że częstotliwość pracy przetwornicy jest precyzyjnie dopasowana do częstotliwości rezonansowej obwodu elektrycznego przetwornicy. W ostatniej części artykułu opisano praktyczne wykonanie zintegrowanej topologii LLC oraz zbadano wpływ niedopasowania pomiędzy częstotliwością pracy przetwornicy a częstotliwością rezonansową na przebiegi prądu i napięcia, charakterystyki wzmocnienia napięciowego, sprawność oraz temperaturę pracy kluczowych elementów przetwornicy mocy.

Słowa kluczowe: energoelektronika, rezonansowe przetwornice AC/DC, bezprzewodowe systemy przesyłania mocy, praca niezależna od obciążenia, termografia

Rafał Kasikowski, PhD Eng.

rafal.kasikowski@p.lodz.pl
ORCID: 0000-0002-2815-1746

He received the M.Sc. degree in electrical engineering in 2002 from the Technical University of Czestochowa, Poland, and he has also earned the M.Sc. degree in energy engineering in 2013 from the University of East Anglia, Norwich, United Kingdom. In 2021 he received the PhD degree in electronics from Lodz University of Technology, Poland, where he is currently working as a postdoctoral researcher. His research interests include modelling and optimization of Switch Mode Power Supplies.